NASA TECHNICAL NOTE

NASA TN D-2633

NASA TN D-2633

EXPERIMENTAL INVESTIGATION OF JET IMPINGEMENT ON SURFACES OF FINE PARTICLES IN A VACUUM ENVIRONMENT

by Norman S. Land and Leonard V. Clark

Langley Research Center

Langley Station, Hampton, Va.

NATIONAL AERONAUTICS AND SPACE ADMINISTRATION • WASHINGTON, D. C. • FEBRUARY 1965

EXPERIMENTAL INVESTIGATION OF JET IMPINGEMENT

ON SURFACES OF FINE PARTICLES IN

A VACUUM ENVIRONMENT

By Norman S. Land and Leonard V. Clark

Langley Research Center
Langley Station, Hampton, Va.

NATIONAL AERONAUTICS AND SPACE ADMINISTRATION

EXPERIMENTAL INVESTIGATION OF JET IMPINGEMENT

ON SURFACES OF FINE PARTICLES IN

A VACUUM ENVIRONMENT

By Norman S. Land and Leonard V. Clark
Langley Research Center

SUMMARY

The erosion characteristics of a bed of fine particles under vacuum conditions $\left(10^{-4} \text{ torr}\right)$ resulting from an impinging jet exhaust were investigated for various particle sizes and jet heights above the dust surface. The investigation included measurements of the craters during erosion, measurements of the visibility reduction, and photographs of the erosion process.

The results of this investigation indicate that there exists a finite jet height above which particles will not be eroded. This height, for given nozzle conditions, varies with surface-particle size. In addition, the results indicate that the magnitude of surface erosion also depends on surface-particle size; erosion is most rapid with the coarsest particles. These and other associated test results are presented and compared with available theory.

INTRODUCTION

Although the gross structure of the visible lunar surface (such as craters and peaks) is well known and directly observable, little is known of the fine structure and no means are currently at hand for definitive remote observation. The present limit of resolution for earth-based optical observation is about 1/8 mile (ref. 1). Recently, the optical resolution has been improved through the pictures taken by Ranger VII to reveal objects on the order of 1 foot in size. These pictures do not directly enable the measurement of the fine surface roughness. However, electromagnetic (ref. 2) and thermal observations (refs. 2 and 3) of the lunar surface suggest that this surface is covered with a layer of insulating material having a roughness between 10 and 300 microns. It is hypothesized from these observations that the surface of the moon is either covered, wholly or partially, by loosely packed dust (ref. 4) or consists of a random cellular, vesicular structure (ref. 5). The validity of this hypothesis will be tested in the future by the Surveyor project or by some type of penetrometer project. Because a deep, loosely packed layer of dust would seem to offer extreme hazards to a manned lunar landing, such a surface has been assumed

in many theoretical and experimental studies of the landing dynamics of touchdown.

An additional problem associated with landing on a layer of dust is its behavior while being subjected to the impingement of a supersonic rocket blast, such as the retrograde rocket to be used for LEM. Some theoretical studies (refs. 6 to 10) have been made of the behavior of the dust under such conditions and also some qualitative experimental work has been reported (refs. 11 to 14). The most complete theoretical treatment of the problem is that given in reference 10 which predicts the time history of crater growth and changes in visibility. The experimental study reported herein was made principally to gather quantitative data to compare with the theory of reference 10.

Measurements were made of the time history of crater growth and the "near-field" visibility with fine particles of various sizes. The experiments utilized a single, supersonic, "cold-gas" nozzle mounted with the jet axis perpendicular to the dust bed. The apparatus was installed and the tests were conducted in the Langley 60-foot-diameter vacuum sphere at the Langley Research Center. A qualitative description of the flow field as gained from the theory and experiments is given in the section following the symbols.

An auxiliary study of the flow field of a supersonic jet impinging onto a smooth, flat plate was also made to determine the ambient pressure required for reasonable simulation, and the results are given in appendix A.

Consideration has been given to the scaling of such experiments (appendix B) but the results of these tests should not be regarded as simulating any specific full-size system.

SYMBOLS

a	speed of sound
c	packing factor
C_f	aerodynamic friction coefficient
d	particle diameter
d_n	nozzle-exit diameter
d_B	diameter of normal shock bowl
g	acceleration due to gravity
h	height above undisturbed surface to nozzle exit
i	tube current

k	constant, $\mu = kT^n$
l	length
m	mass
M	Mach number
n	exponent, $\mu = kT^n$
p	pressure
p_j	static pressure at jet exit
p_s	surface pressure
p_t	total pressure in nozzle plenum chamber
p_∞	ambient pressure in vacuum chamber
r	radial position
r_n	nozzle-exit radius
R	gas constant
N_{Re}	Reynolds number
t	time
T	absolute temperature
V	velocity
v	voltage
y	depth below undisturbed surface
α	angle of repose
γ	ratio of specific heats
λ	length scale, $\dfrac{l_F}{l_M}$
μ	viscosity; also symbol for micron (0.001mm)
ρ_g	mass density of gas

ρ_s mass density of surface material

Δ normal shock standoff distance

$\doteq$ dimensional equivalence

Subscripts:

M   model

F   full size

QUALITATIVE DESCRIPTION OF THE FLOW FIELD

The exhaust flow field of a jet is depicted schematically in a plane section taken through the jet axis in figure 1. Since the moon is believed to be practically devoid of any atmosphere, the jet will operate in an "underexpanded" condition; that is, the static pressure at the jet exit will greatly exceed any ambient pressure. Under such conditions, the jet plumes out, or expands, at a very large angle with respect to the jet axis. Most of the energy, however, is confined to a narrow core as evidenced from the pressure data in reference 11. Also under these high expansions no transverse or oblique shock waves are formed in a free jet.

Just above the surface, a bowl-shaped shock occurs which turns the flow radially outward. Where the extended axis of the jet intersects the surface, a stagnation condition exists. The static pressure along a radial line on the surface decreases rapidly from the stagnation pressure as radial distance from the stagnation point 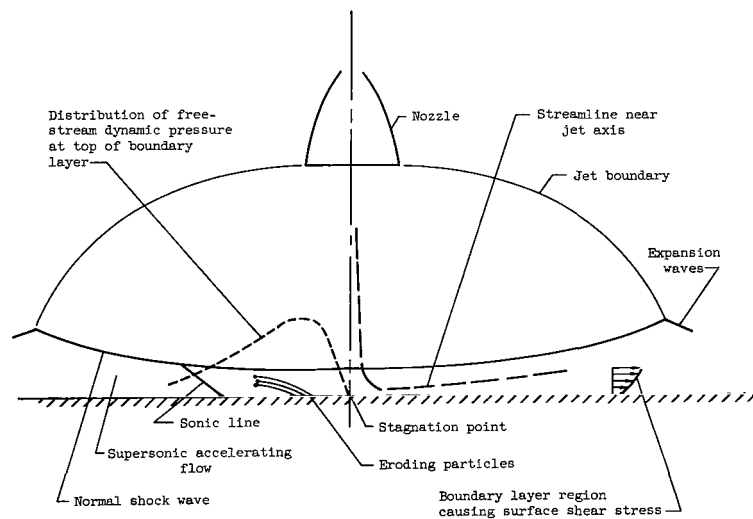increases. The flow just above the surface boundary layer is accelerating radially from zero speed at the stagnation point and reaches supersonic speeds while continually decreasing in density. At some radial location a condition of maximum dynamic pressure is reached. At this location the maximum surface shearing stress is likely to occur. Thus, the dust may be expected to erode initially in an annular ring as verified experimentally in references 11 and 13. With a low nozzle height, the erosion should extend radially with time both inward and outward from the initial ring. The dust ejected from the crater

Figure 1.- Plane section of exhaust flow field of jet.

will move upward and outward in a sheet which, near the surface, resembles an inverted and truncated cone. The ejection velocities may be high and it is theoretically possible for the eroded particles to reach lunar orbital condition. (See refs. 15 and 16.)

APPARATUS AND TEST PROCEDURE

Nozzle

An isentropic expansion nozzle with an exit diameter of 1 inch designed for a Mach number of 3.36 operating with a gas having $\gamma = 1.4$ (an expansion ratio of 5.96) was used for the tests. This particular nozzle was dictated from the scaling considerations given in appendix B. Air was supplied through a solenoid-operated valve to the nozzle at measured stagnation pressures ranging from 11.6 to 16.2 psia and temperatures ranging from 50° to 70° F. Nozzle instrumentation consisted of pressure and temperature gages to provide a measure of nozzle-stagnation conditions and exit pressure.

In an effort to eliminate surface-erosion effects which could be attributed to a starting transient, two techniques were employed whereby dust impingement would result only from a fully established flow. In one technique, the jet exhaust impinged upon a deflector plate located between the nozzle exit and the test bed until nozzle flow had become established. This technique, however, still presented an unrealistic starting transient, since the exhaust suddenly impacted the surface after the deflector plate was moved aside which resulted in high initial erosion and in associated visibility impairment. A second technique was then employed wherein flow was started with the nozzle at a sufficient height above the dust bed to eliminate surface erosion due to the starting transient and then dropped and arrested at a desired height above the surface by means of crushable honeycomb arresters. This latter technique is more representative of the real case of the LEM retrograde rocket braking the vehicle to a soft lunar landing.

Test-Bed Material

The majority of the tests were conducted with particles of aluminum oxide (alumina) in a form used commercially as an abrasive. This material was selected because it is relatively inert and is available in closely graded sizes. Most of the particles are roughly spherical in form although many elongated particles were encountered. One test was conducted on a bed of pumice, which is a porous volcanic glass. The pumice particles appear fibrous in structure with a large percentage of needlelike shapes. In addition, two tests were made with different grades of clean foundry sand.
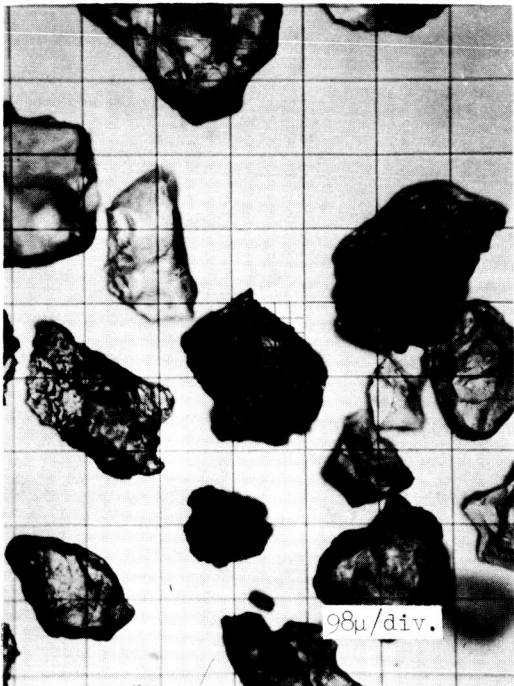
The appearance of the various particles used is illustrated in the photomicrographs of figure 2. The specific gravity of the materials (solid) was measured by a standardized liquid displacement technique which is described in reference 17. The following specific gravities were obtained: pumice, 2.20;
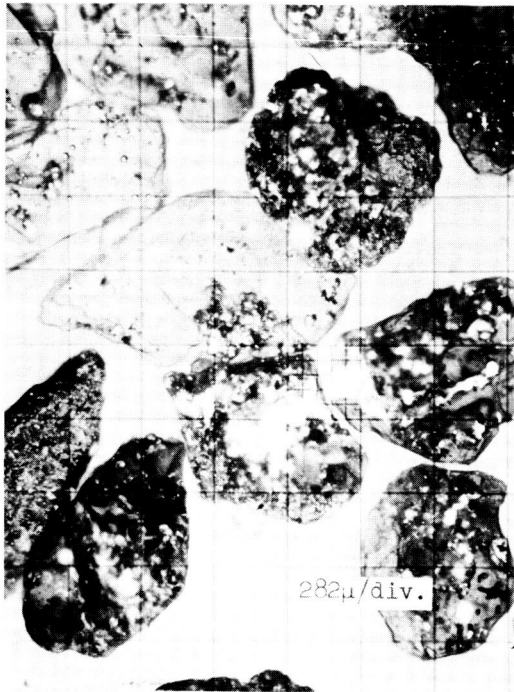
Aluminum oxide ($d_{mean} = 543\mu$)
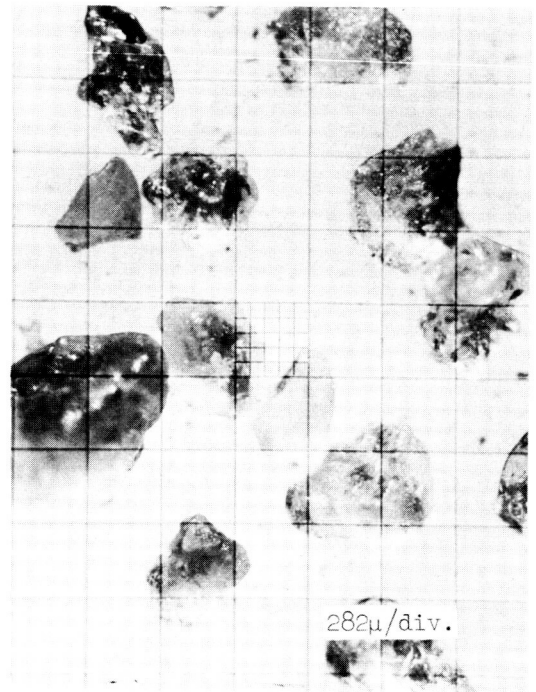
Sand ($d_{mean} = 268\mu$)
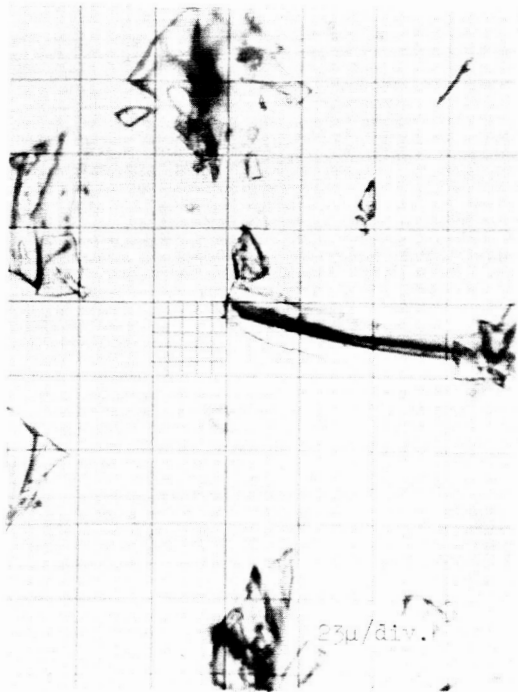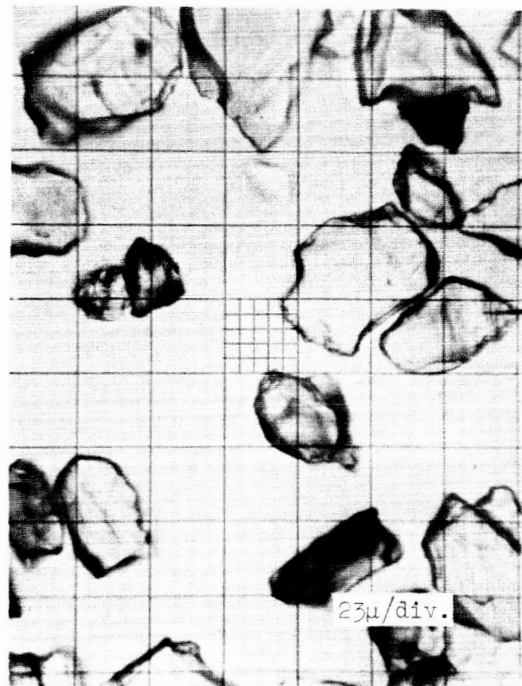
Sand ($d_{mean} = 121\mu$)

Aluminum oxide ($d_{mean} = 75\mu$)

L-64-8392

Figure 2.- Photomicrographs of dust surfaces used for erosion studies.

Pumice ($d_{mean} = 68\mu$)

Aluminum oxide ($d_{mean} = 34\mu$)

Aluminum oxide ($d_{mean} = 4\mu$)

Aluminum oxide ($d_{mean} = 1\mu$)

Figure 2.- Concluded.

L-64-8393

sand, 2.59; and aluminum oxide, 3.89. The particle size distributions were primarily obtained by sieving methods. Sizes greater than 37μ were obtained by using ASTM standard sieves as described in reference 18. Some finer "micromesh" sieves with nominal opening sizes of 5, 10, 15, 20, 25, and 30μ were also used. The sample sizes varied between 150 and 200 grams and were sieved for at least 9 minutes. These sieving procedures are in accordance with the recommendations of reference 19 (pp. 51-52). The sieves were agitated on an automatic sieve shaker which imparted three-dimensional motion. The vertical component had an amplitude of 1/8 inch peak to peak and was operated at 600 cpm which resulted in peak accelerations of 0.64g. The finer grain-size materials (d below 50μ) were also analyzed for their average grain size with an instrument which operates on an air permeability principle (ref. 19, pp. 384-385). The two finest materials were also sized by a standardized microscope counting technique described in reference 20. The results of the sizing measurements are given in figure 3.

Prior to each test the dust beds were prepared to a depth ranging from 3/8 to 6 inches, depending on the type of test. Deep dust beds (4 to 6 inches) were used in the cratering tests. The thin layer was used to determine an incipient erosion boundary as a function of surface-particle size. The materials were placed within a circular form in beds that were 3 to 6 feet in diameter with no deliberate packing and then screeded to provide a relatively smooth surface. For the coarser sizes of particles, the screeded surface is believed to have been smooth to the magnitude of the particle size. The beds composed of the two finest sizes (4μ and 1μ average) could not be screeded to a comparable smoothness because the cohesive forces caused dragging or tearing of the surface.

Facility

The tests were performed in the Langley 60-foot vacuum sphere which has the volume and pumping capacity to permit a reasonable running time at high

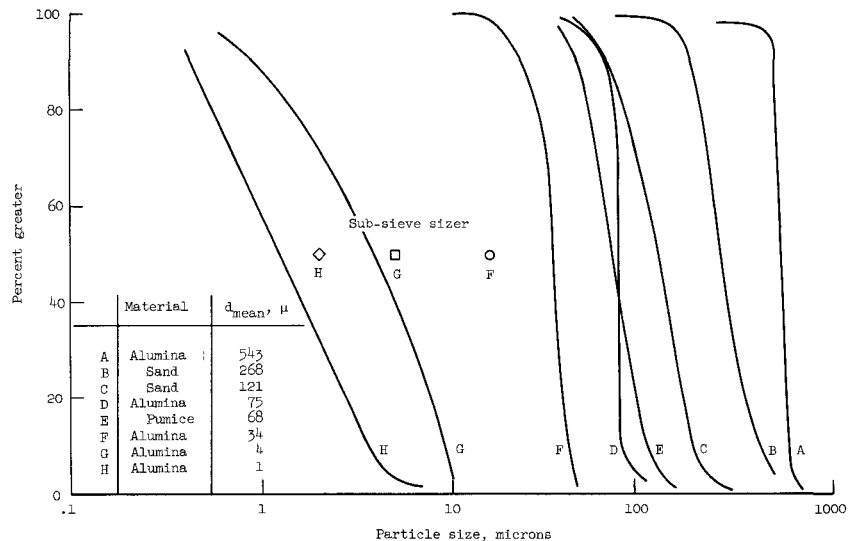|	Material	d_{mean}, μ
A	Alumina	543
B	Sand	268
C	Sand	121
D	Alumina	75
E	Pumice	68
F	Alumina	34
G	Alumina	4
H	Alumina	1

Figure 3.- Grain-size distributions of dust surfaces used for erosion studies.

exit-to-ambient-pressure ratios. The sphere has an ultimate pressure capability of 3×10^{-4} torr after approximately 8 hours of pumping which, following a 26-second test run with the 1-inch-diameter nozzle would increase to approximately 1×10^{-2} torr. These ambient pressures are believed to be low enough to compact the fine particles as shown in reference 21. The jet-exit-to-ambient-pressure ratios corresponding to these pressures would change from 4×10^{4} to 1×10^{3} for a nozzle chamber pressure of 13 psia. In view of the findings of reference 21 and the preliminary supersonic impingement studies performed on a flat plate (appendix A), it appeared that these pressure ratios permitted a reasonable simulation of the pressure environment for investigating erosion on a simulated lunar surface. Initial and final sphere pressures were determined with an ion gage or a McLeod gage. In order to prevent contamination of the 60-foot vacuum sphere pumping equipment by the abrasive dust, the facility was fitted with covers that closed over the diffusion pump inlets; prior to a run, the covers were remotely lowered into place.

MEASURING EQUIPMENT AND TECHNIQUES

Visibility Measurement

The visibility measurements of the present tests were objective in nature as they consisted of recording the resulting attenuation of directed light beams. Subjective visibility measurements (as in ref. 14), were not within the scope of this investigation as they would depend on such factors as contrast, familiarity, and size. In addition, the behavior of the dust was photographically recorded; however, no attempt was made to correlate the objective visibility measurements with these films to obtain subjective visibility measurements. The visibility measurement consisted of recording the output of a photocell which looked at a collimated beam of light originating at the other end of the desired visibility path. (See fig. 4.) The light beam was 5/8 by 13/16 inch in cross section. The beam was attenuated by the debris resulting from surface erosion and the photocell recorded this attenuation through the test. The general setup is shown schematically in figure 4.
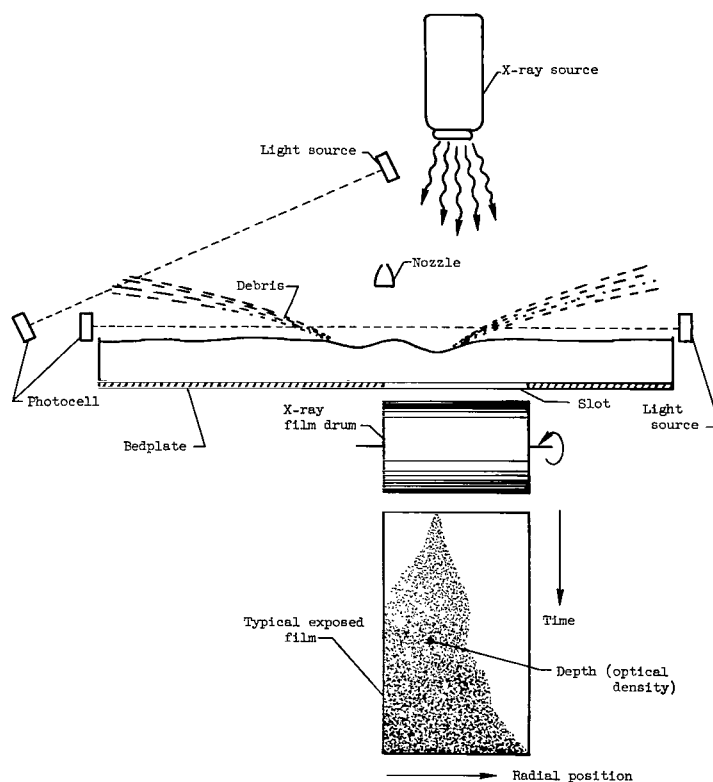

Figure 4.- Schematic of setup.

Visibility through the dust cloud was measured along a path parallel to the surface of the dust bed and also along a path extending from a point just above the nozzle down to a point at the undisturbed surface. The horizontal visibility path was 3 inches above the bed and 3 inches offset from a bed diameter (the nozzle was located at the center of the circular bed); however, for tests to establish incipient erosion boundaries, this path was lowered to 1 inch. The angular visibility path originated from a point 17 inches above the test bed and extended to the undisturbed surface at a depression angle of approximately 23° from the horizontal. This angular sight path is believed to be representative of that used by the pilots of vehicles descending vertically during landing maneuvers.

In performing the visibility measurements, it was necessary to make provisions to eliminate possible "blacking out" of the subject due to coating and/or "sand blast" effects of the test-bed particles on the instrumentation. Coating of the lens and phototube surfaces was held to a minimum by introducing a fine jet of air which washed across these surfaces during a test. The "sand blast" effect of the coarser particles was minimized by employing replaceable cover-glasses over these surfaces.

Dust-Depth Measurement

Dust depth during the transient erosion process was measured by an X-ray absorption technique. This technique is rather unusual and is given special attention in appendix C.

The setup is shown in the sketch of figure 4. An X-ray machine (200 kilovolts, 5 milliamps maximum rating) was positioned above the dust bed at one side of the nozzle. All the unwanted X-rays were essentially stopped by a 3/4-inch-steel plate which formed the bottom of the bed of dust. This plate had a radially positioned slot 3/16 inch wide and 18 inches long, one end of which was near the center line of the nozzle. Underneath this slot was a lead-covered drum 12 inches in diameter, with its axis parallel to the slot, on which a standard 14- by 17-inch sheet of X-ray film was placed. This drum rotated at 2 revolutions per minute. Thus, the time resolution was approximately 0.2 second. This lower assembly was enclosed in lead (except for the slot) to minimize scatter effects. A point on an exposed film in this setup then had coordinates of radial distance and time; the optical density at this point would be a measure of the depth of dust above it. A sketch of a typical film record of the evolution of a crater is included in the setup schematic in figure 4. This system then gives a time history of dust depth over a radial slice of a crater.

The effects of X-ray tube current and voltage on film density for various depths of 34μ aluminum oxide are shown in figure 5. The nonlinear relation between optical density and dust depth is apparent from the figure.

Photographic Coverage

Photographic coverage of the erosion process was accomplished through the use of two high-speed motion-picture cameras and one sequence camera.
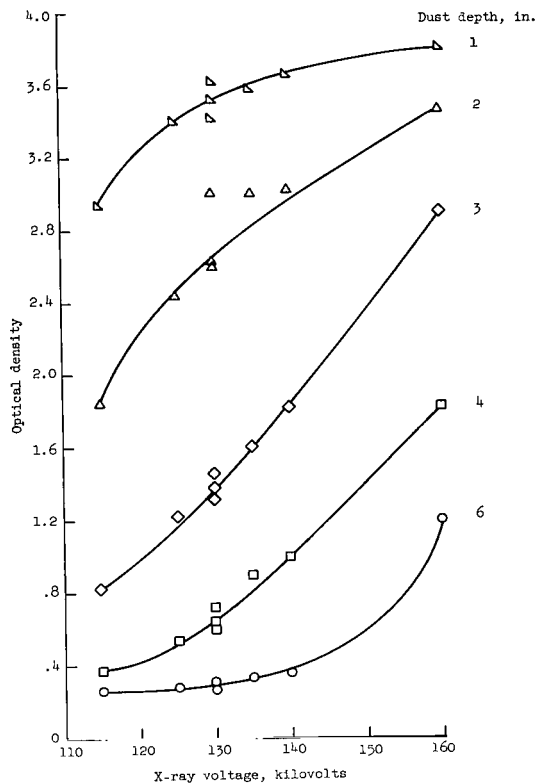
(a) Sensitivity to tube voltage;
  i = 5 milliamps.
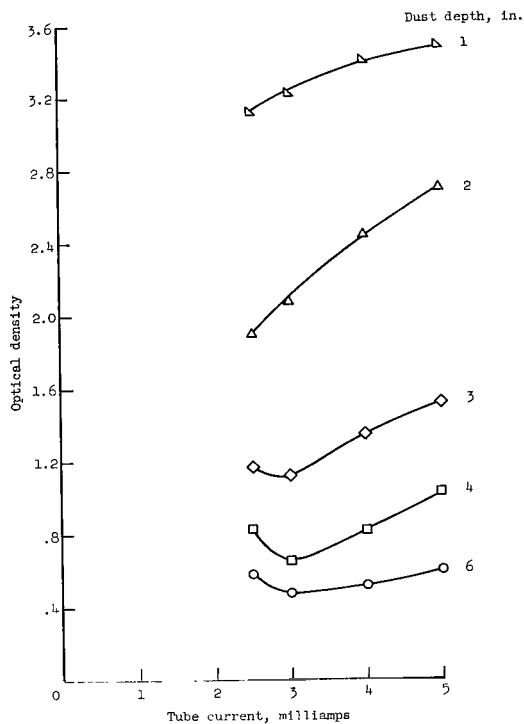
(b) Sensitivity to tube current;
  v = 130 kilovolts.

Figure 5.- X-ray film sensitivity to X-ray tube operating parameters for dust surfaces composed of 34μ aluminum oxide particles.

RESULTS AND DISCUSSION

The results of experimental studies of the effects of a supersonic jet impinging onto surfaces of fine particles under a vacuum-pressure environment are presented in figures 6 to 19. These figures include curves and photographs which describe the behavior of the dust surfaces under such conditions. The jet-exit-to-ambient-pressure ratio for these studies was in the range from 4×10^4 to 1×10^3.

Incipient Erosion Boundary

A particle lying on a surface exposed to a parallel airstream is acted upon by two sets of forces: (1) the air forces on the particle which tend to move it downstream, and (2) the forces between the particle and the surface which tend to restrain it. Since the airstream forces increase with stream dynamic pressure and the particle-surface forces are independent of stream velocity, there must be some minimum airstream velocity required to overcome the static restraining forces and move the particle. Thus, for a given nozzle flow and particle size, it is reasonable to expect that there would be some

11

height of the nozzle above which the particle would not move since the dynamic pressure decreases with height, that is, no erosion would occur.

There are two kinds of static restraining forces: (1) friction, and (2) cohesion. The friction force varies as the particle weight (therefore, as the volume for a constant mass density). The interparticle cohesive forces, about which there is little information, arise from intermolecular attraction and are believed to vary inversely with particle diameter. Large-particle restraining forces will then be dominated by friction and small particle restraining forces, by cohesion. Experience has indicated (ref. 21) that with particles below approximately 15μ, the cohesive forces become dominant. In the large-particle (noncohesive) range, an increase in size results in an increase in the minimum airstream dynamic pressure (or correspondingly, a decrease in nozzle height) necessary to initiate erosion. In the small-particle (cohesive) range, a decrease in particle size requires an increased minimum dynamic pressure (or a corresponding reduction in nozzle height) to initiate erosion - this is shown to be the case experimentally.

The results of tests made to define the erosion boundary of the nozzle exhausting onto aluminim oxide particles are given in figure 6. The experimental data confirm the existence of an incipient erosion boundary and that the boundary shape is as conjectured. The boundary was difficult to determine visually and the nozzle height at which erosion started was not always detectable by visual observation even with the aid of binoculars. The existence of erosion was, however, detected by the visibility measuring system. The erosion points in figure 6 represent less than 4-percent reduction in visibility along a path approximately 7 feet long and 1 inch above the surface of the bed.
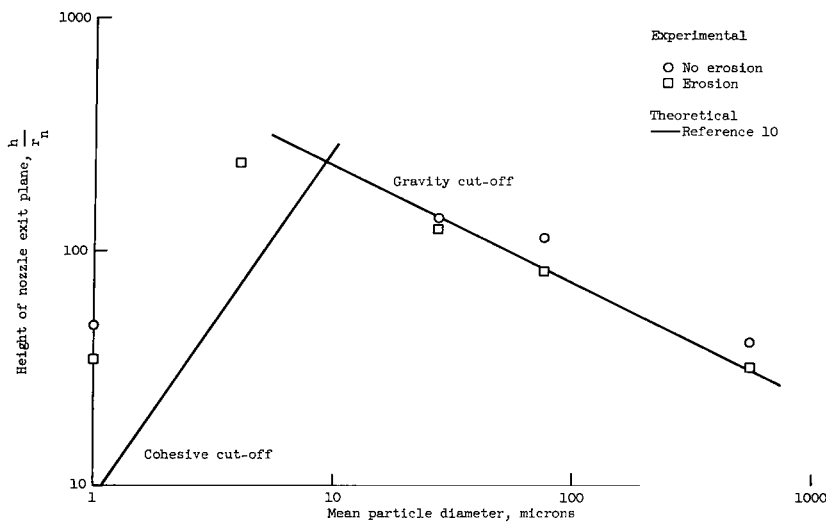

Figure 6.- Incipient erosion boundary for aluminum oxide particles.

One set of theoretical boundaries is shown in figure 6 for comparison with the experimental data. The boundaries are based on the assumption that the surface is very rough (roughness on the order of boundary-layer thickness) and that the aerodynamic shear stress varies as $C_f \rho V^2$. The rough-surface assumption agrees closely with the experimental data. It is indicated then that the theory based on a rough-surface condition should be used even though the surface is visualized as being relatively smooth (as though screeded).

Effect of Particle Size

on Erosion

When the nozzle height is below that for incipient erosion, the aerodynamic shear stress on the surface is greater than the maximum shear stress that the surface can withstand. Momentum will then be transferred from the air-stream to the particles, setting them into motion. There is a definite amount of momentum available for erosion depending on the nozzle height relative to the incipient erosion height, and all this momentum will transfer to particle momentum. As the particle size increases, the inertia (volume) increases faster than the aerodynamic propelling forces (area). Since the larger particles accelerate more slowly than small particles, and therefore attain a smaller fraction of the airstream velocity in a given time than do the smaller particles, a larger mass of the larger particles must erode in a given time in order to absorb the excess momentum. For a given nozzle height, as the size of the particles increases, the erosion will increase until, of course, the erosion boundary is reached in which case erosion stops and all airstream momentum is again absorbed in surface shear stress by the static restraining forces.

Crater profiles determined by using the X-ray system are shown in figures 7 to 12, with time as a parameter, for several sizes and types of dust and three nozzle heights. In each of these figures depth and radial position are non-dimensionalized by using the nozzle radius. The nozzle exit is also
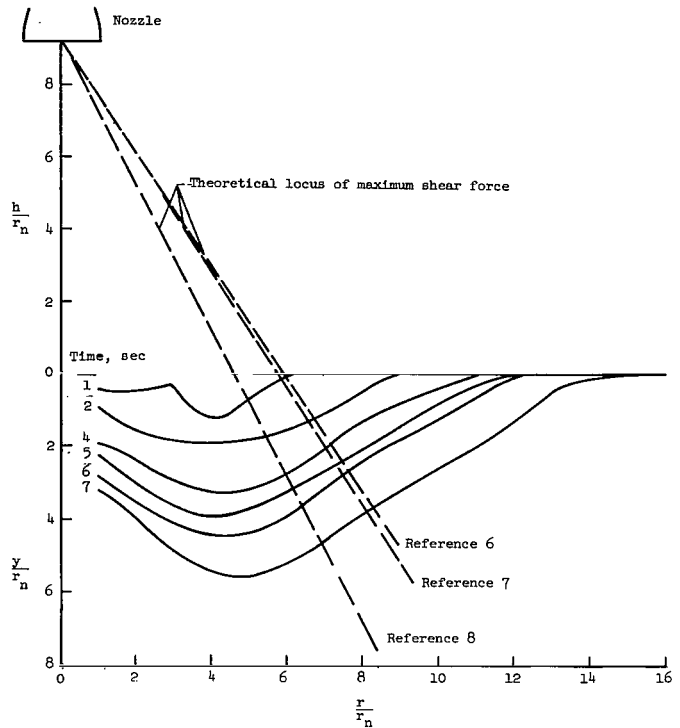

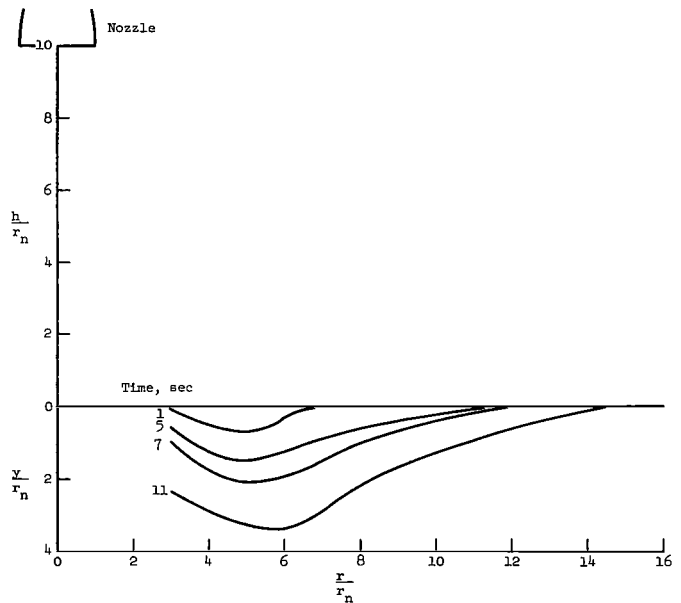Figure 7.- Crater formation in 543μ aluminum oxide particles at $\frac{h}{r_n}$ = 9.2.

Figure 8.- Crater formation in 268μ sand particles at $\frac{h}{r_n}$ = 10.

13
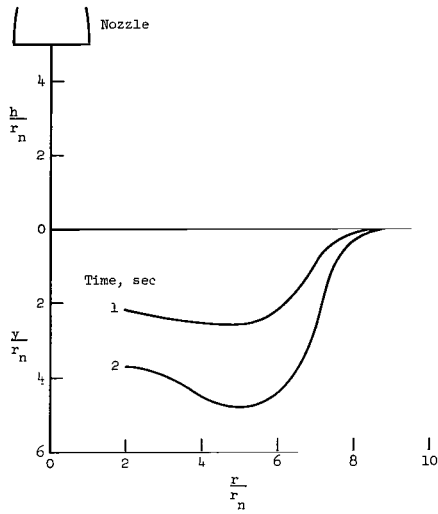
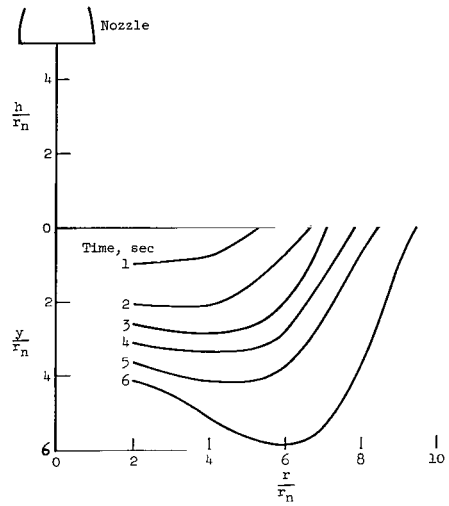Figure 9.- Crater formation
in 268μ sand particles at
$\frac{h}{r_n} = 5.$

Figure 10.- Crater formation
in 121μ sand particles at
$\frac{h}{r_n} = 5.$

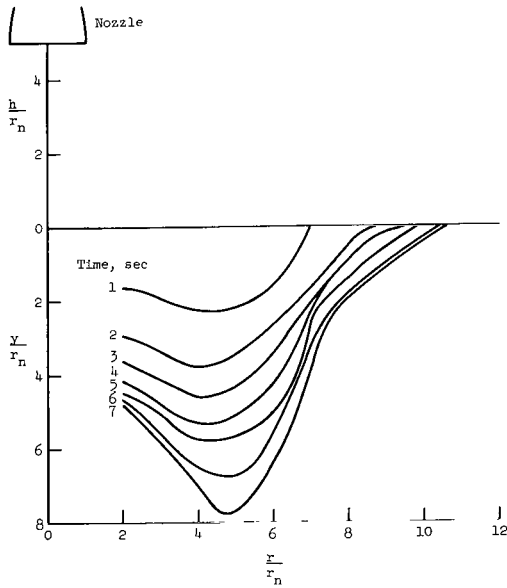Figure 11.- Crater formation
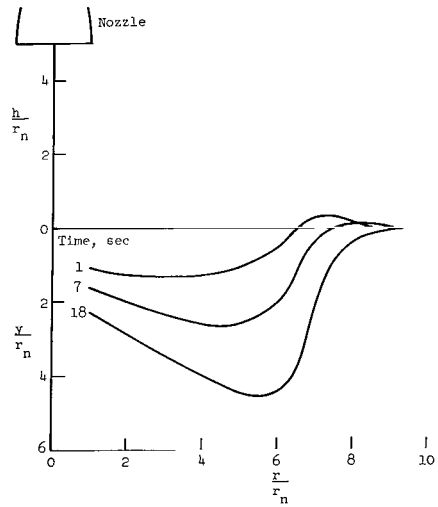in 68μ pumice particles
at $\frac{h}{r_n} = 5.$

Figure 12.- Crater formation
in 1μ aluminum oxide par-
ticles at $\frac{h}{r_n} = 5.$

14

shown in each figure at the appropriate height and size. Crater profiles could not be determined at, or close to, the center because the nozzle and its plenum chamber blocked the X-rays in this region.

In general, the crater profiles tend to support the qualitative description given earlier and the theoretical descriptions, in that there is a maximum erosion some distance out from the center and a resulting central cone. The loci of maximum surface aerodynamic shear stress, as given by the theoretical treatments of references 6 to 8, are shown in figure 7 for comparison with the experimental data.

The erosion-time curves obtained from these data (at a radial location $r/r_n = 4$) are shown in figure 13. Some of the curves presented in figure 13 are not faired through zero erosion at zero time mainly because of erosion due to flow transient effects which occurred before the defined zero time.

The crater profiles of figures 7 and 8 and the erosion-time curves shown in figure 13(a) illustrate the effect of particle size on erosion for a nozzle height of approximately 10 radii. Figures 9 to 12 and the erosion-time curves of figure 13(b) show the particle-size effect for a nozzle height of 5 radii. The decrease in erosion with a decrease in particle size from 543 to 68μ is evident. Although this particle-size range was covered with three materials (sand, pumice, and aluminum oxide), it is believed that within the accuracy of these tests the particle size was the important variable.

The very low erosion rate for the 1μ particle size, as shown by the erosion-time curve of figure 13(b), is believed to be evidence of the interparticle attractive forces (cohesion) which are large compared with gravity forces for fine particles.

A comparison of figures 8 and 9 shows the greatly increased erosion rate as the nozzle height is decreased. A decrease in nozzle height from 10 to 5 radii increased the erosion rate by a factor of approximately 10.

There is an apparent tendency for the craters formed with the low nozzle height to have a greater depth-to-diameter ratio than the craters formed with the higher nozzle height.
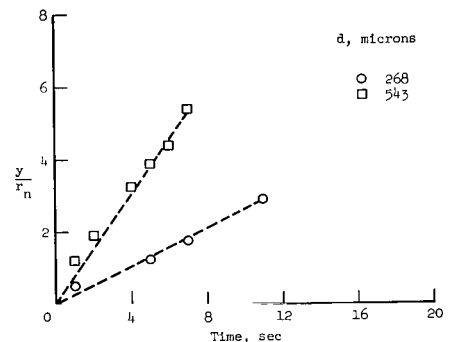
(a) $\dfrac{h}{r_n} \approx 10$.
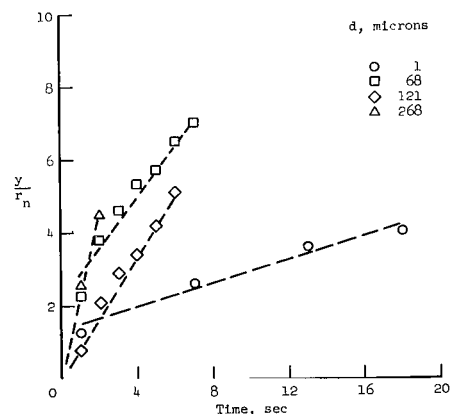
(b) $\dfrac{h}{r_n} = 5$.

Figure 13.- Erosion rates at $\dfrac{r}{r_n} = 4$.

This effect is seen by comparing the shapes of the profiles in figures 7 and 8 with those of figures 9 to 12.

Figure 14 shows experimental erosion rates determined along the theoretical locus of maximum scrubbing action of reference 8 as a function of nozzle height above the dust surface. The limited experimental data are compared with the erosion rates computed by the theory of reference 10. Both the theory and the experimental data are shown for the initial nozzle-to-surface relationship; on this basis the theory overpredicts the rate of formation of the craters. However, as the surface erodes, the nozzle height would effectively increase. Using a more realistic value of nozzle height would greatly improve the agreement between theory $\left(\text{a function of } h^{-5/2}\right)$ and experiment.

Effect of Cohesive Force on Erosion

Figures 15 to 17 present sequential photographs of some of the test runs. The dashed line in the $t = 0$ photograph of these figures indicates the line along which the crater profile was determined. These figures illustrate the effect of interparticle cohesive force on erosion. Figure 15 presents time-sequence photographs of the erosion of a surface with a mean particle diameter of 543μ at a nozzle height of 9.2 nozzle exit diameters. For the same nozzle height figures 16 and 17 present time-sequence photographs of the erosion of 4μ and 1μ particles, respectively. Figure 15 illustrates how the surfaces
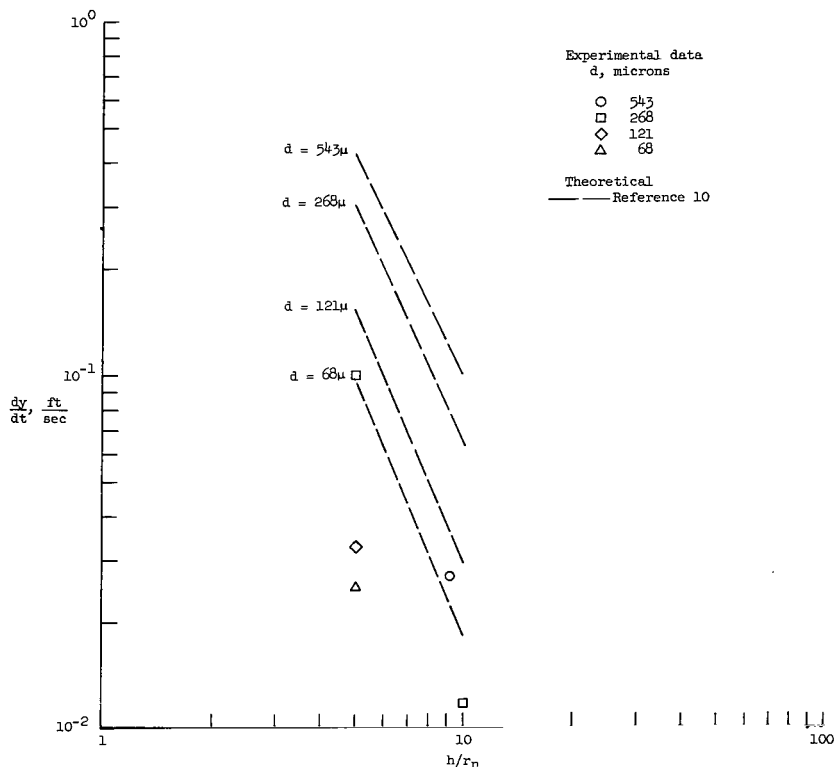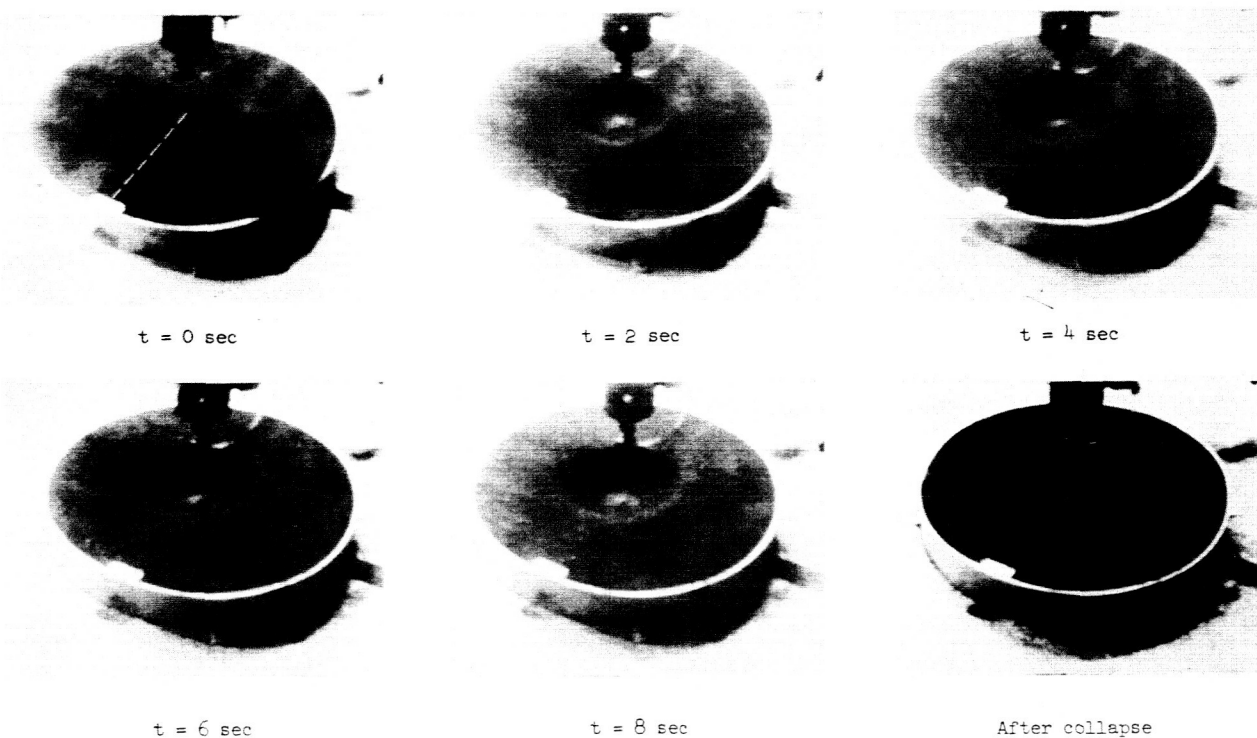

Figure 14.- Variation of erosion rate with nozzle height
and surface particle size.

t = 0 sec   t = 2 sec   t = 4 sec

t = 6 sec   t = 8 sec   After collapse

L-64-8394

Figure 15.- Sequence of photographs showing erosion of 543μ aluminum oxide particles at $\frac{h}{r_n}$ = 9.2.

composed of the larger grains erode evenly, resulting in a crater which is symmetrical about the surface stagnation point. Visible in figure 15 is the central cone at the nozzle stagnation region that was discussed previously. In addition, the walls of the crater may be at angles greater than the static angle of repose of the material (being held there by the exhaust pressure field) and an inward collapse of the crater occurs when the nozzle flow ceases. Figures 16 and 17 show the retarding effect of interparticle cohesive force on erosion. In figure 16 the craters exhibit symmetry about the nozzle center line; however, the surface appears to erode from a finite number of points instead of evenly as in figure 15. Erosion of this surface produces a pronounced ray pattern. The crater profiles (fig. 7) shown pictorially in figure 15 would be representative of any radial section through the crater. This, however, is not true for the case depicted in figure 16 because of the peculiar erosion pattern. The X-ray path through the crater might go through a ray crest or a ray trough and hence the magnitude of the crater profile might differ. Figure 17 shows the behavior of a surface composed of still smaller particles (1μ). The increase of interparticle cohesive force with the decrease in particle size produces another characteristic type of crater. In this instance the erosion appeared to start at a number of finite points around the stagnation region as in figure 16, but the erosion was more pronounced at one particular region. Erosion of this surface produced an asymmetric crater. For the tests onto surfaces of 4μ particles and 1μ particles, the craters were destroyed when the nozzle flow ceased, unlike the tests on the 543μ-particle surface where the sides of the crater merely slumped to the angle of repose. An explanation may be that some of the exhaust is forced into the surface in

17

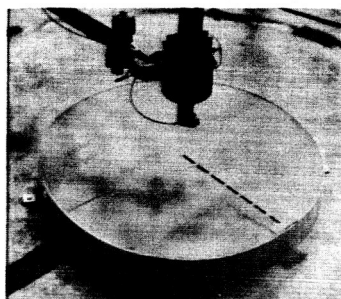|		
t = 0 sec	t = 2 sec	t = 4 sec
t = 6 sec	t = 8 sec	After collapse
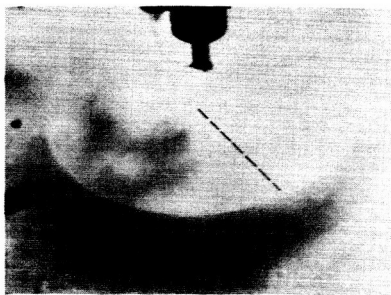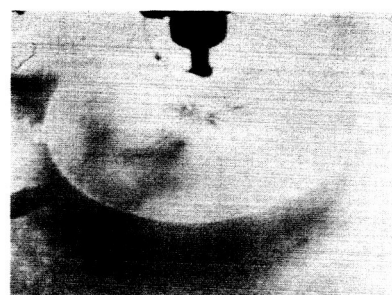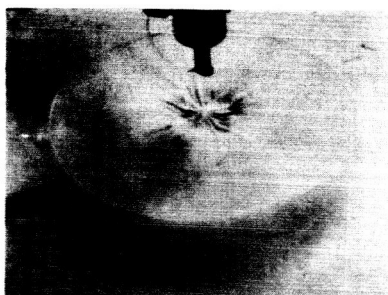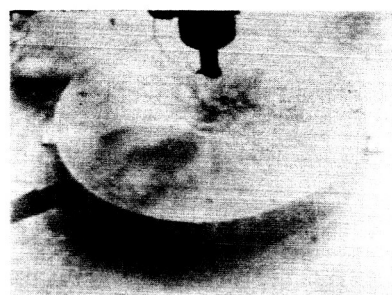
Figure 16.- Sequence of photographs showing erosion of 4μ aluminum oxide particles at $\frac{h}{r_n}$ = 9.2.

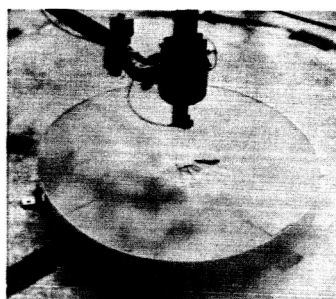|		
t = 0 sec	t = 2 sec	t = 4 sec
t = 6 sec	t = 8 sec	After collapse

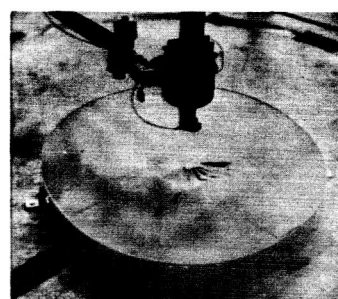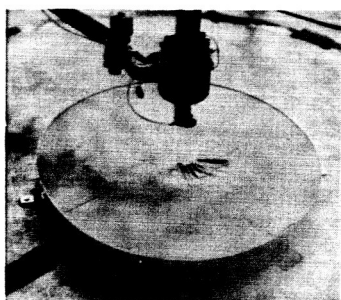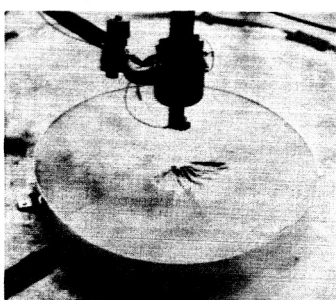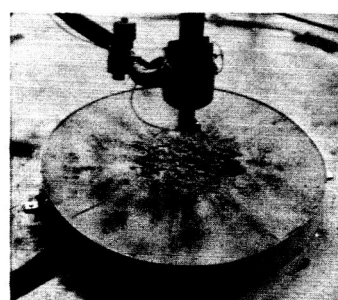Figure 17.- Sequence of photographs showing erosion of 1μ aluminum oxide particles at $\frac{h}{r_n}$ = 9.2.

18

the stagnation region, and when nozzle flow ceases, this air in the test bed expands to the surrounding vacuum and in doing so disturbs the craters. The larger particles would not be affected by this phenomena as the pores between particles are large enough to permit the surface to "breathe" without disturbing the crater.

Effect of Erosion on Visibility

Visibility profiles were obtained for several erosion tests. These profiles consisted of the recorded time history of the attenuation of directed light beams. Figure 18 presents one of these time histories of visibility for the jet exhaust impinging onto $d = 268\mu$ sand particles at a nozzle height of $5r_n$. The mean level of visibility is shown; the actual data had a ± 7-percent high-frequency variation. One-hundred-percent visibility denotes that all the directed light beam is received by the photocell and 0-percent visibility denotes that none of the light is received. This particular profile is shown because during the test the jet exhaust had eroded to the underlying bedplate and the visibility record clearly indicated a subsequent increase in the mean level of visibility. Also seen in the figure is a sharp reduction in visibility at the start of the record as a result of the nozzle starting procedure (establishing flow and then moving a deflector plate aside to let the exhaust impinge onto the surface).

A summary of some of these data is shown in figure 19 as a function of surface-particle size for two nozzle heights. The experimental data represent an average of the visibility level throughout the test runs prior to eroding to the bedplate. The position of the directed light beam for the data is shown in the sketches at the right of the figure. The dashed lines in the figure simply tie the appropriate data together as the data are insufficient to show the variation of visibility with surface-particle size. The lower line ($h/r_n = 5$) shows average visibility levels for a horizontally directed light beam $3d_n$ above the surface and $3d_n$ to one side of the nozzle. The middle line shows data for a higher nozzle height above the dust surface ($h/r_n = 9.2$) where the light beam path is again horizontal, but in this instance only $1d_n$ above the surface. The top line is for corresponding data at $h/r_n = 9.2$ for the angular visibility path looking from a point above the nozzle down to the undisturbed surface at an angle of approximately 23°. The visibility level for the angular path should be and
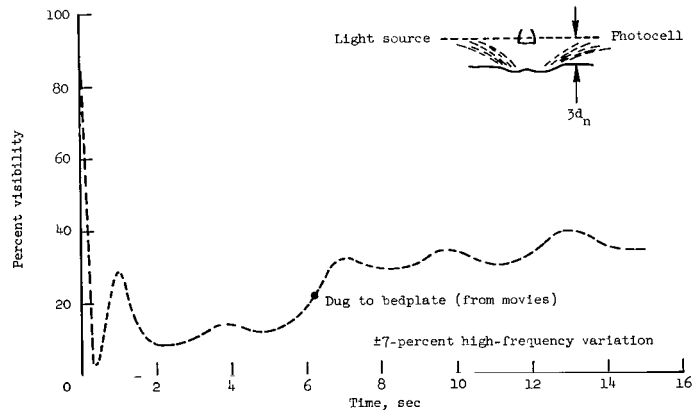

Figure 18.- Mean visibility during erosion of 268μ sand particles at $\dfrac{h}{r_n} = 5$.
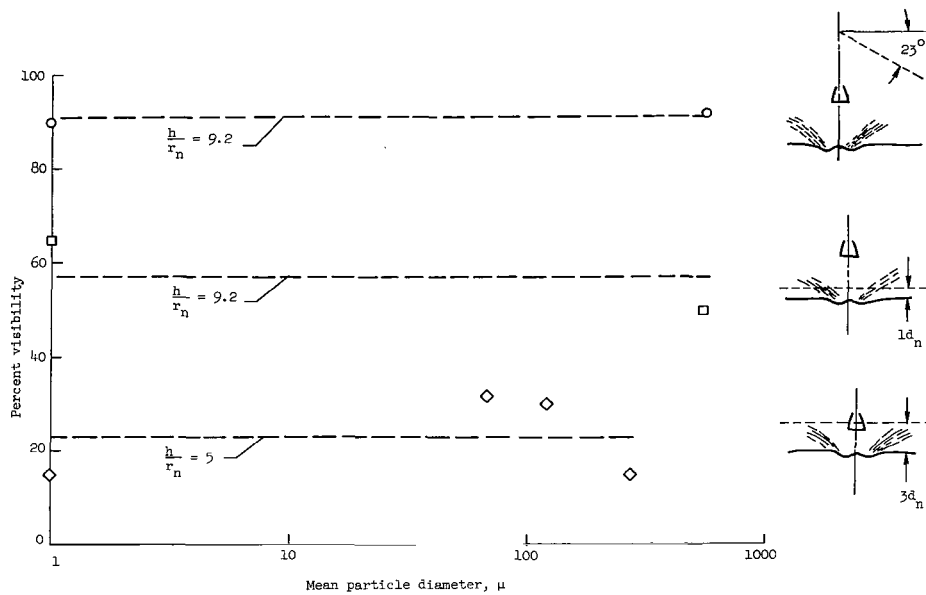
19

Figure 19.- Variation of average visibility with nozzle height and
surface-particle size.

is higher than the horizontal paths because the angular path looks through
only one sheet of crater debris.

CONCLUDING REMARKS

An experimental study has been made of the behavior of fine particles
when subjected to the impingement of a supersonic jet in a vacuum environment.
The tests were limited in extent and were made to gather data to compare with
an existing theory. The tests are not to be regarded as directly representa-
tive of any particular full-size configuration. The results of these tests
indicate the following conclusions:

1. There is a finite nozzle height above which particles will not be
eroded. This height, for given nozzle conditions, varies with the surface-
particle size. Theory based on rough surface or "dynamic" conditions is in
good agreement with this height boundary.

2. The craters that were formed evolved from an initial ring which expanded
radially both inward and outward with time. Prior to collapse the crater is
bowl shaped with sides which may exceed the angle of repose. When nozzle flow
ceases, the crater may collapse. Theory adequately predicts the rate of forma-
tion of the craters.

3. Within the range of the test variables, erosion was most rapid with the
coarsest particles. However, there is a limit to the maximum size of particle
which will erode for a given set of nozzle conditions.

4. Visibility reduction may be especially severe as a result of a sharp nozzle thrust transient. Visibility increases if bottom erosion ceases, that is, when the bottom of a shallow dust layer is exposed.

5. The cohesion forces which exist between particles have an extremely important effect on the behavior of fine particles. Very little information is available on these interparticle forces.

Langley Research Center,
     National Aeronautics and Space Administration,
          Langley Station, Hampton, Va., October 20, 1964.

APPENDIX A

FLOW IMPINGEMENT ON A FLAT SURFACE

Some tests were conducted to determine the ambient pressure required for valid test results and to obtain both a qualitative and quantitative description of the nature of the flow field caused by a supersonic jet impinging normally onto a smooth plate in a vacuum pressure environment. The tests included photographic measurements of the jet boundary and the normal shock formed above the plate at various exit-to-ambient-pressure ratios and measurements of static pressures on the surface.

The basic apparatus, such as the nozzle, valve, and vacuum tank was that which had been used for the tests of reference 14. The vacuum tank had a volume of approximately 5000 ft^3 and could be pumped down to a pressure of approximately 1 torr. The nozzle employed in these tests was designed to have an exit Mach number of 5.0, with an exit diameter of 5/8 inch, and had a 15° half-cone angle expansion section. The nozzle was supplied with nitrogen from bottles pressurized to approximately 2000 psig through a remotely controlled fast-acting valve.

Nozzle stagnation pressure was measured at the entrance to the nozzle and recorded on an oscillograph. Vacuum-tank pressure at the wall near the nozzle was detected by a thermopile pickup and similarly recorded. Static pressures on the plate were measured by miniature diaphragm variable-reluctance gages connected by short lengths of tubing to 0.010-inch-diameter flush orifices in the plate. These pressures were also recorded on the oscillograph. The ratios of exit static pressure to ambient pressure were calculated by using the measured ambient pressure and the exit static pressure computed from the design nozzle Mach number and the measured stagnation pressure.

Shadowgraphs of the flow field were obtained by photographing through a pair of windows in opposite walls of the tank. A beam of light produced by a commercial, 25-watt zirconium concentrated-arc point source at the focus of a parabolic mirror entered the tank through one window and was adjusted to be parallel to the surface of the plate. The beam emerged through the opposite window and was photographed by a lensless aerial camera. The pressure records and shadowgraphs were correlated by having the shutter of the camera electrically connected to the oscillograph.

Figure 20 presents shadowgraphs obtained with the nozzle at 6.7 exit radii above the plate for various jet-exit-to-ambient-pressure ratios. The oblique and normal shocks usually shown in the exhaust field of a free jet at low pressure ratios (see ref. 22) do not appear here probably because of the insensitivity of the shadowgraph system. The shock standoff distances above the plate at the jet center line were measured from these and similar photographs and are plotted in figure 21 as a fraction of the nozzle height as affected by pressure ratio and nozzle height. Shown for comparison are the predicted center-line shock heights for an infinite p_j/p_∞ by the theories of
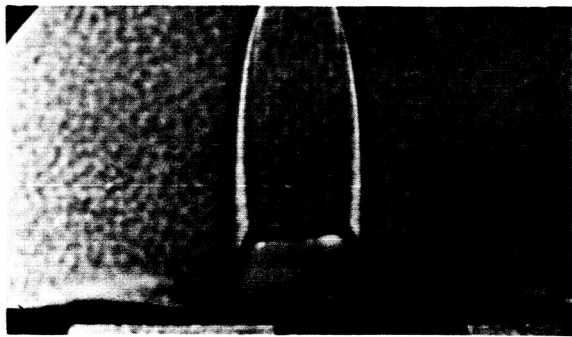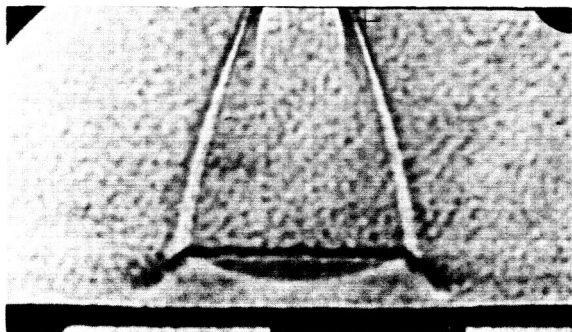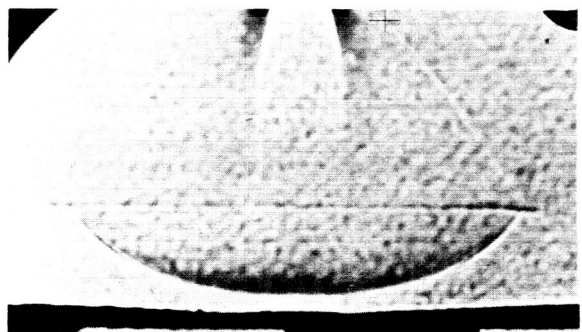
$$\frac{p_j}{p_\infty} = 1.16$$
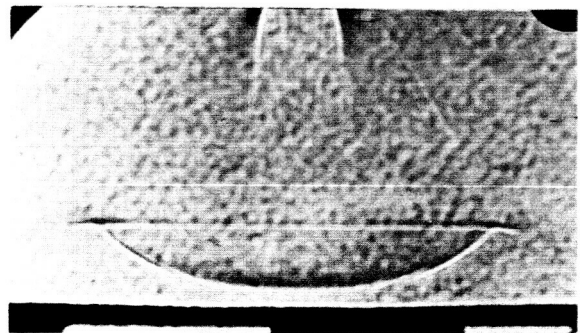
$$\frac{p_j}{p_\infty} = 49.9$$

$$\frac{p_j}{p_\infty} = 3.79$$

$$\frac{p_j}{p_\infty} = 264$$

L-64-8397

Figure 20.- Shadowgraphs of a $M = 5$ jet exhausting onto a flat plate for $\frac{h}{r_n} = 6.7$ under a vacuum pressure environment.

references 6, 7, 8, and 13 which show that the ratio of Δ/h does not vary with height. The experimental data show that the shock height decreases with decreasing nozzle height and that the shock height for a given nozzle height approaches a constant with increasing exit-to-ambient-pressure ratio. The theories of references 6 and 8 are in fair agreement with the data, whereas the theories of references 7 and 13 predict too great a shock standoff height. Figure 21 also shows that the shock standoff distance for a given nozzle height increases sharply as the pressure ratio of the jet approaches an optimum expansion ratio $\left(p_j/p_\infty = 1\right)$. Therefore, these data indicate the necessity of conducting erosion tests, for example, at a high exit-to-ambient-pressure ratio.

The diameter of the bowl-shaped normal shock is shown as a function of pressure ratio for several nozzle heights in figure 22. Within the range of the data, the diameter increases as the nozzle-exit-to-ambient-pressure ratio increases. This can also be seen in the shadowgraphs of figure 20. In addition, the shock diameter for a given nozzle height appears to approach a constant value for increasing pressure ratio in a similar manner as the shock heights presented in figure 21.
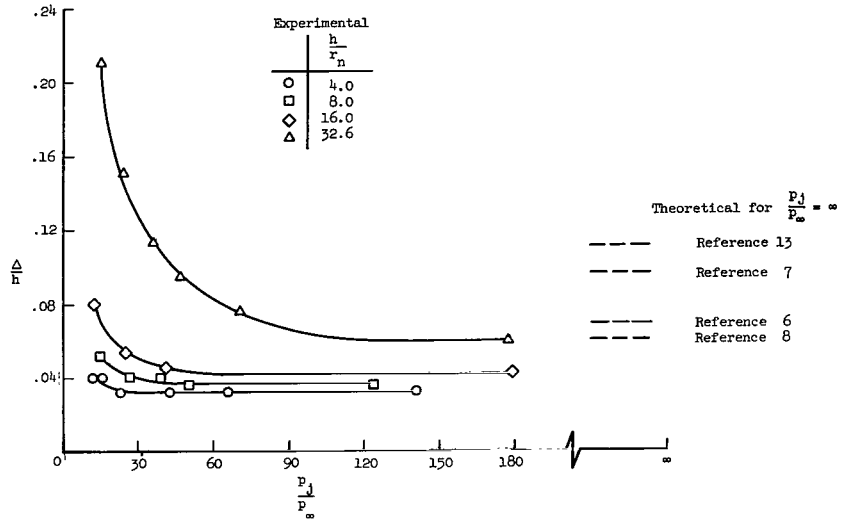
23

Figure 21.- Variation of normal shock stand-
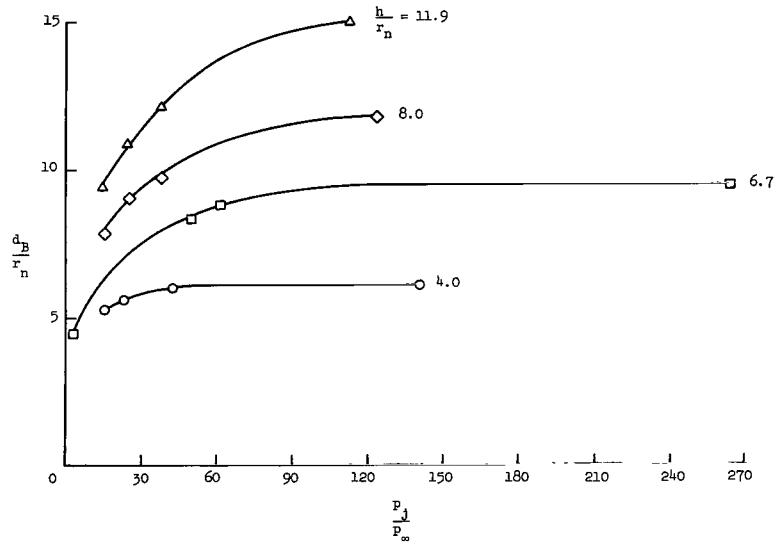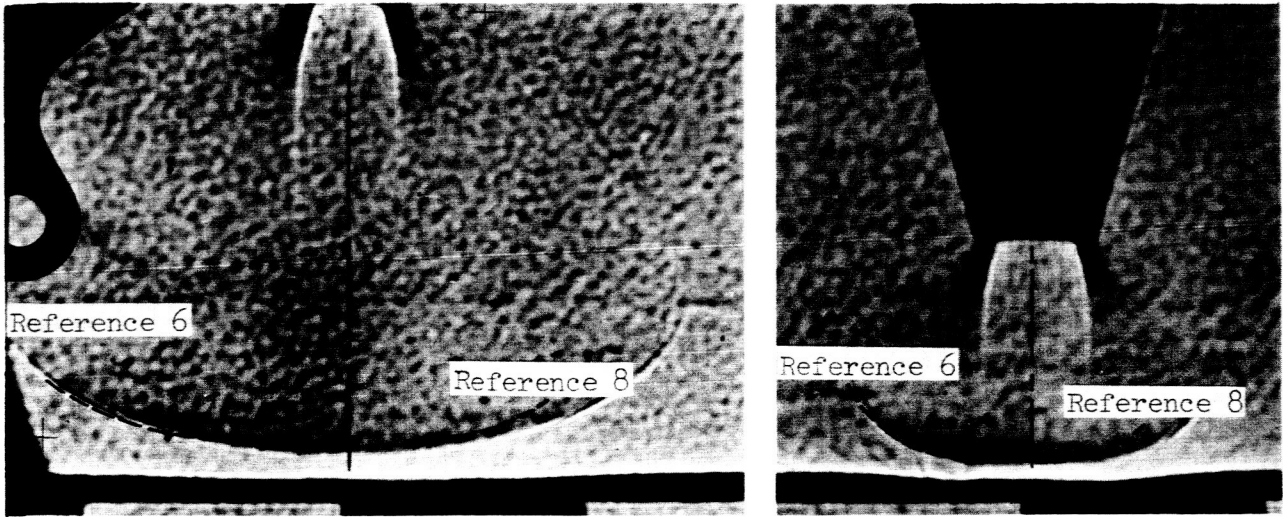off distance with exit-to-ambient-pressure
ratio.

Figure 22.- Variation of normal shock bowl diameter
with exit-to-ambient-pressure ratio.

(a) $\frac{h}{r_n} = 8.0$; $\frac{p_j}{p_\infty} = 124$.   (b) $\frac{h}{r_n} = 4.0$; $\frac{p_j}{p_\infty} = 141$.

L-64-8398

Figure 23.- Shadowgraphs of a $M = 5$ jet exhausting onto a flat plate showing a comparison of shock shape with theory.

The cross-sectional shape of some of the shock waves is shown in figure 23. Also presented are theoretical predictions of the shape, as given in references 6 and 8. Within the range of these tests the theoretical shape given by reference 6 is in excellent agreement, while that of reference 8 is in fair agreement.

Some of the surface static pressures that were measured are given in figure 24. Also shown is the pressure variation predicted in reference 8. The agreement between theory and experiment is good.
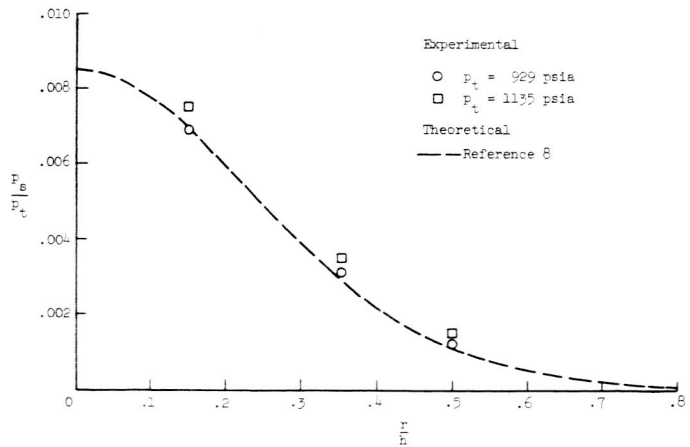

Figure 24.- Surface pressure distribution on a flat plate resulting from an impinging jet at $\frac{h}{r_n} = 8$.

APPENDIX B

SCALING CONSIDERATIONS

It is believed that if similarity between the model and the full-size vehicle for three parts of the erosion problem is achieved, then the overall erosion behavior of the model will reproduce, to scale, the erosion behavior of the prototype. These three parts are: (1) the jet-exhaust flow field, (2) the aerodynamic shear stress on the surface, and (3) the static resistance of the dust to movement.

It is believed, as in reference 10, that the hypersonic similarity parameter $\gamma(\gamma - 1)M^2$ should be the same for model and the full-size vehicle. In addition, the pluming of a jet is governed by the jet-exit cone angle, and the ratio of exit static pressure to ambient static pressure. The jet-exit cone angle is simply handled by geometric similarity, and for the jet tested, this angle was zero in the belief that the angle for the full-size vehicle would be zero also. The ratio of exit to ambient pressure for a full-size lunar vehicle is unknown because the lunar ambient pressure is unknown, but is believed to be very low. The model was tested in a large, low-pressure facility in order to attain a high value of this pressure ratio and a convenient running time. An exact reproduction of the exit-to-ambient-pressure ratio is believed to be unnecessary in view of the tests reported in appendix A.

The aerodynamic shear stress on the surface depends on the type of flow over the surface, which in turn depends on the surface roughness height as compared with the aerodynamic boundary-layer thickness. In reference 10 it is assumed that if the ratio of roughness height to boundary-layer thickness is less than 0.1, laminar flow occurs; if the ratio is between 0.1 and 1.0, the flow is turbulent; and if the ratio is greater than 1, a "dynamic" type of flow occurs. It is believed unlikely that laminar flow will exist for any low nozzle heights. If turbulent flow exists, the surface shear is proportional to $pN_{Re}^{-1/6}$. If the "dynamic" condition exists, the surface shear is of the magnitude of the free-stream dynamic pressure and is proportional to $c_f \rho V^2$.

The static resistance of the dust to movement is composed of two parts: (1) the static friction which is expressed as $\sigma gdc \tan \alpha$, and (2) the cohesion attraction between particles. Two assumptions are made regarding the static friction: (1) the packing factor c is the same for model and the full-size vehicle, and (2) the angle of repose α is the same for model and the full-size vehicle. In this scaling analysis the cohesion forces have been neglected. Little data are available on the magnitude of interparticle cohesion forces on the earth's surface, and none is available on cohesion forces under conditions believed to prevail on the lunar surface.

The erosion of the dust takes place because of a momentum transfer from the gas stream to the dust particles. Therefore, the ratio of mass density of

the gas to the mass density of the dust should be the same for model and full-size vehicle. This is analogous to the mass ratio scaling used in airplane flutter and stability studies.

The conditions for similarity are then believed to be:

Hypersonic flow similarity parameter -

$$\left[\gamma(\gamma - 1)M^2\right]_F = \left[\gamma(\gamma - 1)M^2\right]_M \tag{1}$$

Ratio of particle static friction per unit area to aerodynamic shear stress (turbulent flow) -

$$\left(\frac{\rho_s g d}{p N_{Re}^{-1/6}}\right)_F = \left(\frac{\rho_s g d}{p N_{Re}^{-1/6}}\right)_M \tag{2a}$$

Same ratio as equation (2a) but for a very rough surface -

$$\left(\frac{\rho_s g d}{\rho_g V^2}\right)_F = \left(\frac{\rho_s g d}{\rho_g V^2}\right)_M \tag{2b}$$

Ratio of mass density of gas to mass density of surface material -

$$\left(\frac{\rho_g}{\rho_s}\right)_F = \left(\frac{\rho_g}{\rho_s}\right)_M \tag{3}$$

The scale ratios for length, mass, and time can be determined from equations (1), (2a), and (3) for turbulent flow and equations (1), (2b), and (3) for very rough surface flow. In equation (1), let $M^2 = \left(\frac{V}{a}\right)^2 \doteq \frac{(l/t)^2}{\gamma RT}$. In equation (2a), let $N_{Re} = \frac{\rho_g V l}{\mu}$. In this equation use the relations: $V \doteq l/t$, $\rho_g = p/RT$, and $\mu = kT^n$. Then $N_{Re} \doteq \frac{p l^2}{kRT^{1+n}t}$. Also to avoid a geometrically distorted model, $d \doteq l$.

Length Scale

The length scale as determined from the turbulent flow (eqs. (1) and (2a)) is :

$$\lambda = \frac{l_F}{l_M} = \left(\frac{\rho_{s,M}}{\rho_{s,F}}\right)^{6/7}\left(\frac{g_M}{g_F}\right)^{6/7}\left(\frac{\gamma_F - 1}{\gamma_M - 1}\right)^{1/14}\left(\frac{R_F}{R_M}\right)^{1/14}\left(\frac{T_F^{0.5+n_F}}{T_M^{0.5+n_M}}\right)^{1/7}\left(\frac{k_F}{k_M}\right)^{1/7}\left(\frac{p_F}{p_M}\right)^{5/7}$$

The length scale as determined from the rough surface, or dynamic condition (eqs. (1) and (2b)) is:

$$\lambda = \frac{l_F}{l_M} = \frac{\gamma_M - 1}{\gamma_F - 1}\frac{\rho_{s,M}}{\rho_{s,F}}\frac{g_M}{g_F}\frac{p_F}{p_M}$$

The following values of the various quantities are believed to be representative of the full-size and the experimental study reported herein:

Parameter	Model	Full size
M	3.36	4.5
γ	1.4	1.25
R, ft^2/sec^2-°R	1716	2115
k, lb-sec/ft^2-°R^n	3.4×10^{-9}	2.6×10^{-9}
n	0.76	0.70
g, ft/sec^2	32.2	5.32
σ, lb-sec^2/ft^4	7.5 for aluminum oxide	5.0 average of estimates
p, lb/in.^{2} } Exit	0.21	0.23
T, °R }	163	1760
p, lb/in.^{2} } Stagnation	13	125
T, °R }	530	6200

By using these values, the length scale λ is 11 calculated from the turbulent assumption; and λ is 15.9 on the assumption of "dynamic" conditions.

Time Scale

The first similarity condition (eq. (1)) implied a time scale:

$$\frac{t_F}{t_M} = \left(\frac{\gamma_F - 1}{\gamma_M - 1}\frac{R_M}{R_F}\frac{T_M}{T_F}\right)^{1/2}\lambda$$

Upon substitution of numerical values, the time scale on a turbulent basis is 1.9 and 2.7 for a rough surface condition.

APPENDIX B

Mass Scale

Using equation (3) and the dimensional equivalence ρ_g or $\rho_s \doteq m/l^3$ the mass scale is:

$$\frac{m_F}{m_M} = \frac{\rho_{g,F}}{\rho_{g,M}} \lambda^3$$

or

$$\frac{m_F}{m_M} = \frac{\rho_{s,F}}{\rho_{s,M}} \lambda^3$$

For the tests reported herein, it is of interest to see if the ratios of gas mass density to material mass density are the same for model and full-size vehicle. Substituting the numerical values, these ratios are:

$$\frac{\rho_{g,F}}{\rho_{s,F}} = 1.8 \times 10^{-6}$$

$$\frac{\rho_{g,M}}{\rho_{s,M}} = 1.4 \times 10^{-5}$$

It is apparent that for the model, the gas was heavier relative to the particle material than is the case for the assumed full-size vehicle. It is believed, therefore, that the experimental erosion data presented here should not be used directly to predict the behavior of the Apollo LEM vehicle.

Additional Comments on Scaling

It is believed that the rough-surface, or dynamic, condition is likely to prevail and model tests should be scaled by this scheme. It should be noted that the ratio of the rough-surface aerodynamic shear stress to the static friction per unit area of the dust particles, $\rho_g V^2 / \rho_s gd$, is also the product of the mass ratio of gas to dust material, ρ_g / ρ_s, and a Froude number V^2/gd, which relates inertia to gravity effects. If the Froude number were independently alike for the model and the full-size vehicle, some assurance that the trajectory of the dust particles would be similar for the model and the full-size vehicle could be given.

The Knudsen number which relates the mean-free-path length of gas molecules to a body length has been neglected in this discussion. Referred to mean-free-path lengths calculated for the tank pressures encountered during these tests and average dust particle sizes, the Knudsen number ranged from 2×10^2 to 10^5.

APPENDIX C

X-RAY METHOD OF MEASURING DUST DEPTH

When planning these tests, it was decided that quantitative time histories of dust erosion were a necessity. Two methods were selected for use. One was a photographic technique using stadia rods fastened to the bottom of the bed which would be exposed as erosion proceeded. The other method employed an X-ray absorption technique. Both were tried but only the latter proved successful. Because the X-ray absorption system is rather unusual, it is herein described in detail.

Actually, the first bench tests were made with gamma radiation emitted by a radioactive element. Since the amount of gamma radiation (number of disintegrations) is a random function of time and since the time history of dust depth was the objective, the method proved unsuitable. The radiation output from an X-ray tube, however, is constant and in addition is safer since the radiation source can be electrically deactivated. X-rays are frequently used qualitatively and sometimes quantitatively but seldom to obtain a quantitative time relationship.

The X-ray dose received at some point within the field of the X-ray tube without an absorber between target and reference point is described by the equation (see ref. 23):

$$I_0 = \frac{kiv^c t}{s^2}$$

where I_0 is dose received; k is a constant; i is tube current; v is tube voltage; t is time; s is distance from target to reference point; and $c \approx 2.5$ (value depends on X-ray machine parameters).

When an absorber is placed between the tube target and the reference point, the relation becomes

$$I = I_0 e^{-\mu\rho d/\rho}$$

where I is dose received at reference point with absorber; I_0 is dose received at reference point with no absorber; μ is X-ray linear absorption coefficient; ρ is density of absorber material; and d is depth or thickness of absorber. The quantity μ/ρ is a nonlinear function of the material contained in the absorber and the energy of the rays striking it. The general nature of this function is shown in figure 25. (See ref. 23.) The result is that the dose received at a point below a dust bed is:

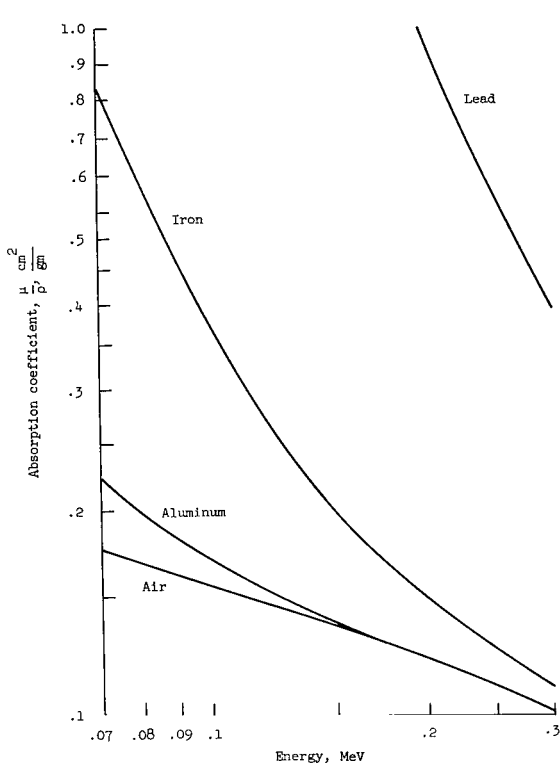$$I = \frac{kiv^c t}{s^2} e^{-\mu\rho d/\rho}$$

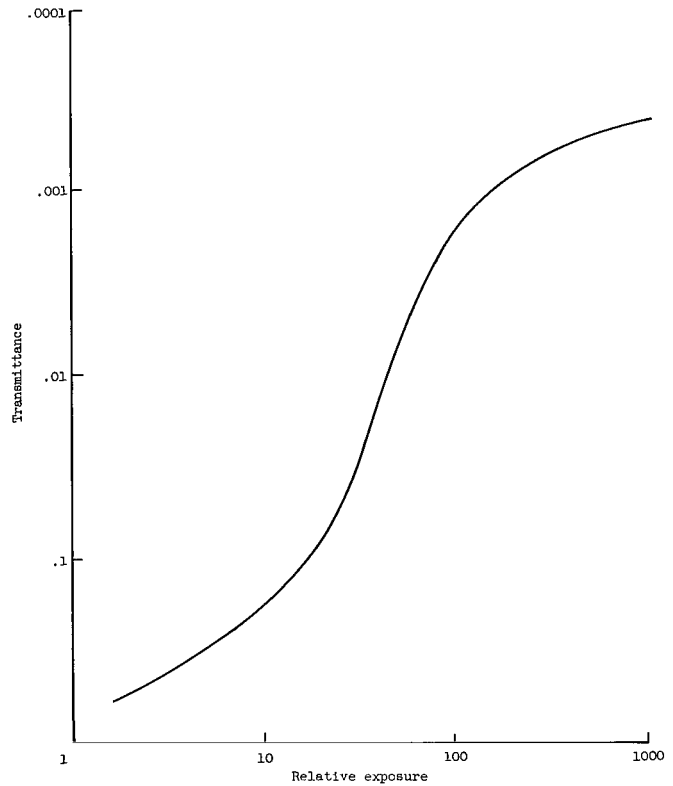Figure 25.- Variation of X-ray absorption coefficient with X-ray energy.

Figure 26.- Typical X-ray film sensitivity. (Replotted from ref. 24.)

Thus, for a given setup, the dose is an exponential function of the dust-bed thickness and a linear function of time.

Consideration must also be given to the nature of the detector. Commercial X-ray film seemed to be a good choice because it could be used to provide a continuous depth survey rather than a point-by-point survey. The sensitivity of the film to X-rays is also a nonlinear function as may be seen in figure 26, which is taken from reference 24. X-ray film sensitivity may be increased by the use of fluorescent intensifying screens which cause an additional optical exposure or by lead screens which reradiate electrons and secondary X-rays and attenuate scatter radiation.

REFERENCES

1. Kuiper, Gerald P.: The Exploration of the Moon. Vol. II of Vistas in
   Astronautics, Morton Alperin and Hollingsworth F. Gregory, eds., Pergamon
   Press (New York), 1959, pp. 273-313.

2. Giraud A.: Characteristics of the Moon's Surface Layer: An Analysis of Its
   Radio Emission. Astrophys. J., vol. 135, no. 1, Jan. 1962, pp. 175-186.

3. Whipple, Fred L.: On the Lunar Dust Layer. Vol. II of Vistas in Astro-
   nautics, Morton Alperin and Hollingsworth F. Gregory, eds., Pergamon
   Press (New York), 1959, pp. 267-272.

4. Gold, Thomas: Dust on the Moon. Vol. II of Vistas in Astronautics,
   Morton Alperin and Hollingsworth F. Gregory, eds., Pergamon Press (New
   York), 1959, pp. 261-266.

5. Green, Jack: The Geology of the Lunar Base. Report No. SID 61-358, North
   Am. Aviation, Inc., Dec. 15, 1961.

6. Edwards, R. H.: Interaction of the Surveyor Vernier Rocket With the Surface
   of the Moon. Hughes Aircraft Co. Ref. 4162.1/34, Apr. 12, 1961.

7. Shepard, G. Dudley: The Effect of Retro-Rocket Exhaust on Visibility
   During Lunar Touchdown. Rept. No. R-391 (Contract NAS9-153), M.I.T.,
   Dec. 1962.

8. Roberts, Leonard: The Action of a Hypersonic Jet on a Dust Layer. Paper
   No. 63-50, Inst. Aerospace Sci., Jan. 1963.

9. Yoshihara, Hideo: Rocket Exhaust Impingement on a Ground Surface. J. of
   Fluid Mech., vol. 15, pt. 1, Jan. 1963, pp. 65-73.

10. Roberts, Leonard: The Interaction of a Rocket Exhaust With the Lunar Sur-
    face. Presented at a Specialists' Meeting on "The Fluid Dynamic Aspects
    of Space Flight" (Marseille, France), AGARD, Apr. 20-24, 1964.

11. Stitt, Leonard E.: Interaction of Highly Underexpanded Jets With Simulated
    Lunar Surfaces. NASA TN D-1095, 1961.

12. Spady, Amos A., Jr.: An Exploratory Investigation of Jet-Blast Effects on
    a Dust-Covered Surface at Low Ambient Pressure. NASA TN D-1017, 1962.

13. Sibulkin, M.; and Gallaher, W. H.: Some Aspects of the Interaction of a
    Jet With a Dust Covered Surface in a Vacuum Environment. Rept.
    ERR-AN-244(Contract No. REA 111-9403), Eng. Dept., Gen. Dyn./Astronaut.,
    Feb. 10, 1963.

14. Hurt, George J., Jr.; and Lina, Lindsay J.: Blast Effects of Twin Variable-Cant Rocket Nozzles on Visibility During Landing on a Particle-Covered Surface. NASA TN D-2455, 1964.

15. Grossman, Robert L.: Characteristics of Particles Blown Away by Exhaust Jet Impingement on a Lunar Surface. Rept. No. ADR 04-04-62.3, Grumman Aircraft Eng., Corp., Dec. 1962.

16. Cramblit, D. C.: A Consideration of Lunar Surface Ballistics and the Hazards Associated With Spacecraft Landing or Launch Operations. NASA TN D-1526, 1963.

17. Anon.: Standard Method of Test for Specific Gravity of Hydraulic Cement. ASTM Designation C 188-44, pt. 4 of 1961 Book of ASTM Standards Including Tentatives. Am. Soc. Testing Mater., c.1961, pp. 190-191.

18. Anon.: Sieves for Testing Purposes. ASTM Designation E 11-61, pt. 4 of 1961 Book of ASTM Standards Including Tentatives. Am. Soc. Testing Mater., c.1961, pp. 1479-1486.

19. Herdan, G.: Small Particle Statistics. Second ed., Academic Press, Inc. (New York), 1960.

20. Anon.: Analysis by Microscopical Methods for Particle Size Distribution of Particulate Substances of Subsieve Sizes. ASTM Designation E 20-62 T, pt. 4 of 1962 Supplement to Book of ASTM Standards Including Tentatives. Am. Soc. Testing Mater., c.1962, pp. 229-240.

21. Clark, Leonard V.; and McCarty, John Locke: The Effect of Vacuum on the Penetration Characteristics of Projectiles into Fine Particles. NASA TN D-1519, 1963.

22. Love, Eugene S.; Grigsby, Carl E.; Lee, Louise P.; and Woodling, Mildred J.: Experimental and Theoretical Studies of Axisymmetric Free Jets. NASA TR R-6, 1959.

23. Kinsman, Simon, compiler and ed.: Radiological Health Handbook. PB 121784 U.S. Dept. Health, Educ., Welfare, Jan. 1957.

24. Anon.: Radiography in Modern Industry. Eastman Kodak Co., c.1947.

NASA SCIENTIFIC AND TECHNICAL PUBLICATIONS

TECHNICAL REPORTS: Scientific and technical information considered important, complete, and a lasting contribution to existing knowledge.

TECHNICAL NOTES: Information less broad in scope but nevertheless of importance as a contribution to existing knowledge.

TECHNICAL MEMORANDUMS: Information receiving limited distribution because of preliminary data, security classification, or other reasons.

CONTRACTOR REPORTS: Technical information generated in connection with a NASA contract or grant and released under NASA auspices.

TECHNICAL TRANSLATIONS: Information published in a foreign language considered to merit NASA distribution in English.

TECHNICAL REPRINTS: Information derived from NASA activities and initially published in the form of journal articles.

SPECIAL PUBLICATIONS: Information derived from or of value to NASA activities but not necessarily reporting the results of individual NASA-programmed scientific efforts. Publications include conference proceedings, monographs, data compilations, handbooks, sourcebooks, and special bibliographies.

Details on the availability of these publications may be obtained from:

SCIENTIFIC AND TECHNICAL INFORMATION DIVISION

NATIONAL AERONAUTICS AND SPACE ADMINISTRATION

Washington, D.C. 20546